

École doctorale n° 364 : Sciences Fondamentales et Appliquées

Doctorat ParisTech

T H È S E

pour obtenir le grade de docteur délivré par

l'École Nationale Supérieure des Mines de Paris

Spécialité doctorale "Science et Génie des Matériaux"

présentée et soutenue publiquement par

Ali SAAD

le xx septembre 2015

NUMERICAL MODELLING OF MACROSEGREGATION FORMED DURING SOLIDIFICATION WITH SHRINKAGE USING A LEVEL SET APPROACH

Directeurs de thèse: **Michel BELLET**
Charles-André GANDIN

Jury

M. Blablabla,	Professeur, MINES ParisTech	Rapporteur
M. Blablabla,	Professeur, Arts Et Métiers ParisTech	Rapporteur
M. Blablabla,	Chargé de recherche, ENS Cachan	Examineur
M. Blablabla,	Danseuse, en freelance	Examineur
M. Blablabla,	Ingénieur, MIT	Examineur

MINES ParisTech

Centre de Mise en Forme des Matériaux (CEMEF)
UMR CNRS 7635, F-06904 Sophia Antipolis, France

Acknowledgement

Dedicated to humanity ...

Contents

1	Energy balance with thermodynamic tabulations	1
1.1	State of the art	2
1.2	Thermodynamic considerations	3
1.2.1	Volume averaging	3
1.2.2	The temperature-enthalpy relationship	4
1.2.3	Tabulation of properties	4
1.3	Numerical method	6
1.3.1	Enthalpy-based approach	10
1.3.2	Temperature-based approach	10
1.3.3	Convergence	11
1.4	Validation	12
1.4.1	Pure diffusion	12
1.4.2	Convection and diffusion	15
1.5	Application: multicomponent alloy solidification	18
1.5.1	Tabulations	20
1.5.2	Discussion	21
	Bibliography	27

Contents

List of Acronyms

Acronym	Standing for
ALE	Arbitrary Lagrangian-Eulerian
BTR	Brittle temperature range
CAFD	Cellular Automata Finite Difference
CAFE	Cellular Automata Finite Element
CBB	Circumventing Babuška-Brezzi
CCEMLCC	Chill Cooling for the Electro-Magnetic Levitator in relation with Continuous Casting of steel
CEMEF	Centre de Mise en Forme des Matériaux
CFL	Courant–Friedrichs–Lewy
C.FL	Computing and FLuids
CSF	Continuum Surface Force
DLR	Deutsches Zentrum für Luft- und Raumfahrt
DSPG	Darcy-Stabilising/Petrov-Galerkin
EML	Electromagnetic levitation
ESA	European Space Agency
FEM	Finite Element Method
FVM	Finite Volume Method
GMAW	Gas Metal Arc Welding
ISS	International Space Station
IWT	Institut für Werkstofftechnik
LHS	Left-hand side
LSIC	Least squares on incompressibility constraint
LSM	Level set method
MAC	Marker-and-cell
PF	Phase field
PSPG	Pressure-Stabilising/Petrov-Galerkin
RHS	Right-hand side
RUB	Ruhr Universität Bochum
RVE	Representative Elementary Volume
SBB	Satisfying Babuška-Brezzi
SUPG	Streamline-Upwind/Petrov-Galerkin
VMS	Variational MultiScale
VOF	Volume Of Fluid

Contents

Chapter 1

Energy balance with thermodynamic tabulations

Contents

1.1 State of the art	2
1.2 Thermodynamic considerations	3
1.2.1 Volume averaging	3
1.2.2 The temperature-enthalpy relationship	4
1.2.3 Tabulation of properties	4
1.3 Numerical method	6
1.3.1 Enthalpy-based approach	10
1.3.2 Temperature-based approach	10
1.3.3 Convergence	11
1.4 Validation	12
1.4.1 Pure diffusion	12
1.4.2 Convection and diffusion	15
1.5 Application: multicomponent alloy solidification	18
1.5.1 Tabulations	20
1.5.2 Discussion	21

1.1 State of the art

To model macrosegregation during solidification, a minimum of four conservation equations are necessary: conservation of mass, momentum, chemical species and energy. The phase change literature contains a wealth of numerical methods to solve energy conservation in solidifying alloys. A comprehensive overview of these methods is given by [Swaminathan et al. \[1993\]](#).

The corresponding equation associates the total average enthalpy to the temperature via intrinsic alloy properties, such as the heat capacity of the phases and the latent heat associated with the phase transformations. However, in the course of solidification and while macrosegregation is taking place, these properties change because the average composition may vary significantly: the transformation paths are thus modified, as well as the phases' composition and heat capacity. Similarly, the latent heat of phase transformations is not a mere constant that could be distributed as a function of the phase fractions assuming only temperature-dependent phases' properties, as often found in the literature [\[Bellet et al. 2009\]](#). It is thus impossible to establish a priori the dependence of the enthalpy with respect to temperature when macrosegregation alters the average composition, even in the case of full thermodynamic equilibrium between phases.

In this chapter, we discuss a suitable numerical scheme based on an enthalpy method, already used in the literature to alleviate this macrosegregation-related problem [\[Swaminathan et al. 1993; Carozzani et al. 2013\]](#). Later on, we introduce a modified formulation, using the effective heat capacity method that increases the original scheme's efficiency.

This chapter introduces an enthalpy method that makes use of a temperature-based solver. It uses tabulated thermodynamic quantities (solidification paths, phases' enthalpy and composition) in a range of average compositions and temperatures as found in the literature [\[Doré et al. 2000; Thuinet et al. 2004; Du et al. 2007\]](#), with the aim of evaluating the total average enthalpy as well as the effective heat capacity. The novelty of the modified method resides in the use of thermodynamic tabulations without losing the advantages of the previous method, thus yielding faster computation times while maintaining a good accuracy.

1.2 Thermodynamic considerations

1.2.1 Volume averaging

The volume averaging technique, presented in ??, is considered when solving the energy equation in the presence of macrosegregation. The reason is that phase properties and distributions varying with the average composition, have a great impact on the average thermal properties, and hence on the overall heat transfer in the system. We recall the basic equation:

$$\langle \psi \rangle = \sum_{\phi} g^{\phi} \langle \psi \rangle^{\phi} \quad (1.1)$$

where g^{ϕ} denotes the volume fraction of phase ϕ in the RVE. It should be emphasized that the averaging technique applies to virtually all thermodynamic volumetric variables (enthalpy, density . . .). Among these variables, the temperature is also considered to be uniform in the RVE.

Applying the volume averaging technique to the energy conservation principle along with interfacial balances between the phases, results in the following averaged equation [Rappaz et al. 2003]:

$$\frac{\partial \langle \rho h \rangle}{\partial t} + \nabla \cdot \langle \rho h \vec{v} \rangle = \nabla \cdot \left(\langle \kappa \rangle \vec{\nabla} T \right) + \langle \dot{Q}_V \rangle \quad (1.2)$$

where ρ stands for the density, h the mass enthalpy, \vec{v} the velocity field, κ the thermal conductivity, T the temperature and \dot{Q}_V a possible volumetric heat source. Equation (1.2) is the standard averaged form of the energy conservation equation used in non-stationary phase change problems.

It is clear that the nature of the temperature-enthalpy relationship plays a central role when formulating the resolution strategy of this nonlinear equation. Generally, it is admitted that, depending on the resolution strategy, it is necessary to express enthalpy as a function of temperature or vice-versa, together with associated partial derivatives, $\frac{d\langle \rho h \rangle}{dT}$ or $\frac{dT}{d\langle \rho h \rangle}$.

It is noted that in the FEM context, the RVE is represented by a node in a finite element, so for instance the temperature in a RVE is denoted T_j henceforth, where j represents the index of the node localising the RVE.

1.2.2 The temperature-enthalpy relationship

In solidification problems, additional variables are involved in [eq. \(1.1\)](#) and [eq. \(1.2\)](#), like the transformation path that defines the history of the phase fractions, as well as the average chemical composition $\langle w_i \rangle$, i being the index of the chemical species (only the solutes are considered). The temperature-enthalpy relation averaged over the phases in a given RVE writes:

$$\langle \rho h \rangle = \sum_{\phi} g^{\phi}_{(T, \langle w_i \rangle \dots)} \langle \rho \rangle^{\phi}_{(T, \langle w_i \rangle \dots)} \langle h \rangle^{\phi}_{(T, \langle w_i \rangle \dots)} \quad (1.3)$$

Note that the volume average enthalpy is approximated by the product $\langle \rho h \rangle^{\phi} = \langle h \rangle^{\phi} \langle \rho \rangle^{\phi}$ in the current work. As stated in the introduction, it becomes clear from [eq. \(1.3\)](#) that phase properties, i.e. average phase density, $\langle \rho \rangle^{\phi}$ and enthalpy, $\langle h \rangle^{\phi}$, are temperature and composition dependent. This equation is the key to convert the average volume enthalpy to temperature (through a procedure named *H2T*) or vice-versa (*T2H*). The values of the different phase fractions g^{ϕ} (solidification path) and phase enthalpies $\langle \rho h \rangle^{\phi}$ are thus needed to close the relation.

1.2.3 Tabulation of properties

The complexity of performing a thermodynamic conversion is directly linked to the simplicity of determining the alloy properties, namely the phase fractions and both phase densities and enthalpies. In the case of binary alloys and with several assumptions with respect to the system (e.g., linear monovariant lines in temperature-composition relationships of the phase diagram, constant heat capacity of phases and constant latent heat of transformations, equilibrium approximations between phases) analytical calculations are often used to determine the phase fractions and phase compositions. Nevertheless, analytical relations are more complex or even impossible to derive in the case of multicomponent alloys ($i > 1$), or even for binary alloys with multiple phase transformations (e.g. peritectic and eutectic reactions) with a nonlinear phase diagram.

To overcome this problem, one can resort to thermodynamic databases and phase equilibrium calculations to tabulate the transformation paths and the phase densities and enthalpies for a given range of temperatures and average compositions. It is a handy solution for two main reasons: first, the conversion is merely a binary search in a table; secondly, it is a simple solution for coupling with macrosegregation. In this way, phase fractions g^{ϕ} are tabulated as functions of temperature and average composition, while for each phase ϕ the mass enthalpy, $\langle h \rangle^{\phi}$, and the density, $\langle \rho \rangle^{\phi}$, are

tabulated as functions of temperature and phase intrinsic average compositions $\langle w_i \rangle^\phi$, as well as other possible parameters.

[Table 1.1](#) summarizes the steps in order to perform a temperature-to-enthalpy ($T2H$) conversion using the predefined tabulation approach. In step 1, the transformation path is acquired for each average composition, $\langle w_i \rangle$, and temperature, T , to determine the list of phases, their volume fractions g^ϕ and their intrinsic compositions $\langle w_i \rangle^\phi$, assuming full equilibrium. In step 2, the phase enthalpy $\langle h \rangle^\phi$ and density $\langle \rho \rangle^\phi$ are determined by searching for the temperature and the already known phase composition $\langle w_i \rangle^\phi$. In step 3, the average volume enthalpy is computed from the volume fraction, density and mass enthalpy of phases using [eq. \(1.3\)](#). A flowchart explaining $T2H$ conversion steps is given in [fig. 1.1](#).

Table 1.1 – Tabulation processing for a $T2H$ procedure

Step Number	1	2	3
Inputs	$T, \langle w_i \rangle$	$T, \langle w_i \rangle^\phi$	$g^\phi, \langle \rho \rangle^\phi, \langle h \rangle^\phi$
Outputs	$g^\phi, \langle w_i \rangle^\phi$	$\langle \rho \rangle^\phi, \langle h \rangle^\phi$	$\langle \rho h \rangle$ (eq. (1.3))

The methodology to build the tabulations is straightforward. It is based on two main scans. On the one hand, intervals for the variation of the average composition $\langle w_i \rangle$ are chosen from the known alloy composition. These variations have to cover the extreme values adopted during the simulation, which are not known a priori. An interval is also selected for the variation of temperature. The latter is easier to determine as it usually starts from the initial melt temperature and goes down to the room temperature in a standard casting simulation. For each mapping of composition and temperature, a thermodynamic equilibrium state is computed. The outputs are the number of phases encountered, together with their fraction and intrinsic compositions. On the other hand, for each phase, a scan of the intrinsic composition and temperature is made to compute the intrinsic properties. The same temperature interval and step as defined earlier are used.

Regarding the enthalpy-to-temperature conversion ($H2T$) shown in the flowchart in [fig. 1.2](#), a backward iterative $T2H$ search is performed. For a known composition $\langle w_i \rangle$, denoting (τ) the iteration index to convert the enthalpy H_{input} , we start with an initial guess for temperature $T^{(\tau=0)}$ then convert it to an enthalpy $H^{(\tau=0)}$ with the $T2H$ conversion. Using an appropriate nonlinear algorithm (Brent is the most versatile in our case), we aim at minimizing the following scalar residual: $R_H = |H_{\text{input}} - H^{(\tau)}|$. Once the algorithm has converged, the temperature $T^{(\tau)}$ is the result of the $H2T$ conversion. It is inferred that the first conversion ($T2H$) is a direct one whereas the latter ($H2T$) is

indirect and requires a series of iterative steps; each step being a single $T2H$ resolution. In other words, a $H2T$ conversion is a backward search for a temperature, hence it is slower. This conversion's speed lag is exacerbated when tabulations increase in size (e.g. large number of temperature and composition steps) and complexity (e.g., multi-component industrial alloys used in casting), since the search gets more complicated with the increasing number of input columns (one column for each alloying element).

Initialisation	
Temperature	T_j
Average composition	$\langle w_i \rangle_j$
Microsegregation law	
Phase fractions	$(T_j, \langle w_i \rangle_j) \rightarrow g_j^\phi$
Phase compositions	$(T_j, \langle w_i \rangle_j) \rightarrow \langle w_i \rangle_j^\phi$
Phase volumetric enthalpy	$(T_j, \langle w_i \rangle_j) \rightarrow \langle \rho h \rangle_j^\phi$
Total enthalpy	
$\langle \rho h \rangle_j = \sum_\phi \left[g_j^\phi \langle \rho \rangle_j^\phi \langle h \rangle_j^\phi \right]_{T_j}$ (eq. (1.3))	

Fig. 1.1 – Algorithm for a single temperature to enthalpy ($T2H$) conversion at node j .

1.3 Numerical method

The finite element method is used to solve the energy conservation as expressed by eq. (1.2). A test function \mathcal{W} belonging to the Hilbertian Sobolev space $\mathcal{H}^1(\Omega_E)$ of continuous integrable test functions is used to formulate the integral variational form of eq. (1.2) [Süli 2000]. A Fourier boundary condition is considered on the domain boundary $\partial\Omega_E$. The domain Ω is discretised using first-order linear simplexes, Ω_E , defined by their number of local nodes, NbLoc: triangles in 2D with NbLoc=3 and tetrahedra in 3D with NbLoc=4. The outcome is a residual that we aim to minimize so that the conservation principle is satisfied. Therefore, the weak form writes:

$$\begin{aligned}
 \forall \mathcal{W} \in M = \{u \in \mathcal{H}^1(\Omega_E)\} \\
 \int_{\Omega_E} \mathcal{W} \frac{\partial H}{\partial t} dV + \int_{\Omega_E} \mathcal{W} \langle \vec{v}^l \rangle \cdot \vec{\nabla} \langle \rho h \rangle^l dV - \int_{\Omega_E} \mathcal{W} \nabla \cdot (\langle \kappa \rangle \vec{\nabla} T) dV - \int_{\Omega_E} \mathcal{W} \langle \dot{Q}_V \rangle dV = 0
 \end{aligned}
 \tag{1.4}$$

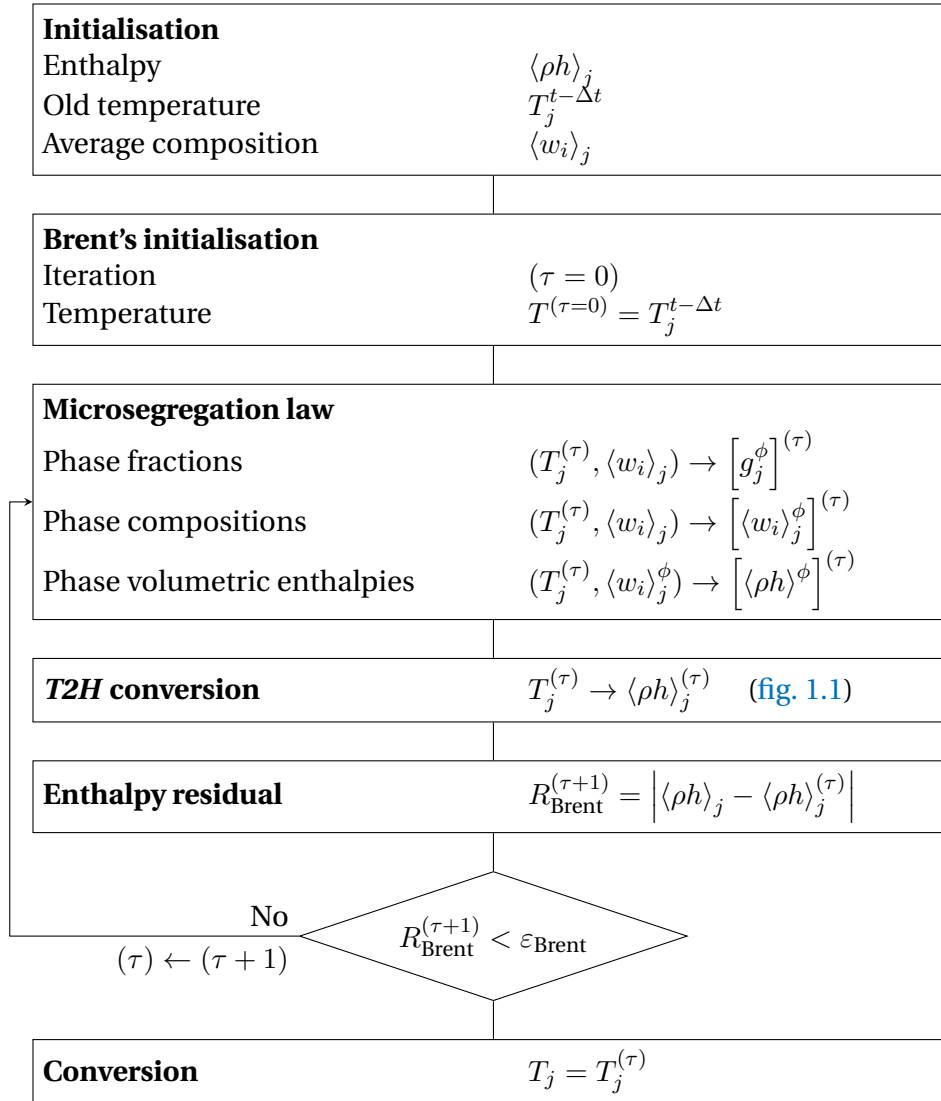


Fig. 1.2 – Algorithm for a single enthalpy to temperature (H2T) conversion at node j .

Chapter 1. Energy balance with thermodynamic tabulations

where $H = \rho h$ is the volumetric enthalpy, introduced to simplify notations in the following. Furthermore, we assumed a static solid phase and an incompressible liquid phase, which allowed recasting the second term of [eq. \(1.2\)](#) into $\langle \vec{v}^l \rangle \cdot \vec{\nabla} \langle \rho h \rangle^l$. $\langle \rho h \rangle^l = \langle \rho \rangle^l \langle h \rangle^l$ is not main variable of the energy conservation equation's weak form, [eq. \(1.4\)](#). Therefore we express it as a function of temperature, which is related to the main variable via the enthalpy-temperature relation:

$$\vec{\nabla} \langle \rho h \rangle^l = \vec{\nabla} \left(\langle \rho \rangle^l \langle h \rangle^l \right) = \langle \rho \rangle^l C_p^l \vec{\nabla} T \quad (1.5)$$

where C_p^l is the mass heat capacity of the liquid phase. Ideally, this value should be taken directly from the thermodynamic database if it is available. Otherwise, it can be derived by differentiation of the tabulated liquid mass enthalpy with respect to temperature. In this work, C_p^l is considered constant, equal to the alloy's initial mass heat capacity. The steps for discretising in time and space [eq. \(1.4\)](#) are well detailed in some text books like [Rappaz et al. \[2003\]](#). As for enthalpy and temperature, they are spatially discretised in each simplex using interpolations functions \mathcal{P} , thus defining the nodal values H_j and T_j , respectively:

$$H = \sum_{j=1}^{\text{NbLoc}} \mathcal{P}_j H_j \quad (1.6)$$

$$T = \sum_{j=1}^{\text{NbLoc}} \mathcal{P}_j T_j \quad (1.7)$$

The Galerkin formulation gives the expression for the residual contribution at a mesh node i (here i is not the usual solute index) for time step t in a local element Ω_E :

$$\begin{aligned} (R_i^E)^t &= \mathcal{M}_{ij}^E \left(H_j^t - H_j^{t-\Delta t} \right) + \mathcal{A}_{ij}^E T_j^t + (\mathcal{K}1_{ij}^E + \mathcal{K}2_{ij}^E) T_j^t - \mathcal{F}_i^E - \mathcal{Q}_i^E = 0 \\ i, j &: 1 \rightarrow \text{NbLoc} \end{aligned} \quad (1.8)$$

where the volumetric contributions are detailed as follows:

$$\text{transient term: } \mathcal{M}_{ij}^E = \int_{\Omega_E} \frac{1}{\Delta t} \mathcal{P}_i \mathcal{P}_j \, dV \quad (1.9)$$

$$\text{advection term: } \mathcal{A}_{ij}^E = \int_{\Omega_E} \langle \rho \rangle^l C_p^l \mathcal{P}_i \langle \vec{v}^l \rangle \cdot \vec{\nabla} \mathcal{P}_j \, dV \quad (1.10)$$

$$\text{diffusion term: } \mathcal{K}1_{ij}^E = \int_{\Omega_E} \langle \kappa \rangle \vec{\nabla} \mathcal{P}_i \vec{\nabla} \mathcal{P}_j \, dV \quad (1.11)$$

$$\text{source term: } \mathcal{Q}_i^E = \int_{\Omega_E} \mathcal{P}_i \langle \dot{Q}_V \rangle \, dV \quad (1.12)$$

while the surface boundary contributions are given by:

$$\text{boundary condition term 1: } \mathcal{K}2_{ij}^E = \int_{\partial\Omega_E} h_{\text{ext}} \mathcal{P}_i \mathcal{P}_j \, dS \quad (1.13)$$

$$\text{boundary condition term 2: } \mathcal{F}_i^E = \int_{\partial\Omega_E} h_{\text{ext}} T_{\text{ext}} \mathcal{P}_i \, dS \quad (1.14)$$

$$(1.15)$$

The surface integrals $\mathcal{K}2_{ij}^E$ and \mathcal{F}_i^E are related to a Fourier-type boundary condition, with h_{ext} as a coefficient of heat exchange and T_{ext} as the external temperature far from the boundary. The energy conservation principle is satisfied when the sum of the residual contributions coming from all the mesh elements is zero. In other words, the following global residual defined by the assembly of these contributions, should be minimized:

$$(R_i)^t = \mathcal{M}_{ij} \left(H_j^t - H_j^{t-\Delta t} \right) + \mathcal{A}_{ij} T_j^t + (\mathcal{K}1_{ij} + \mathcal{K}2_{ij}) T_j^t - \mathcal{F}_i - \mathcal{Q}_i = 0 \quad (1.16)$$

$i, j : 1 \rightarrow \text{NbGlob}$

where the global tensors \mathcal{M}_{ij} , \mathcal{A}_{ij} , $\mathcal{K}1_{ij}$, $\mathcal{K}2_{ij}$, \mathcal{F}_i and \mathcal{Q}_i contain respectively, after an assembly step, the contributions of the local matrices \mathcal{M}_{ij}^E , \mathcal{A}_{ij}^E , $\mathcal{K}1_{ij}^E$, $\mathcal{K}2_{ij}^E$, \mathcal{F}_i^E and \mathcal{Q}_i^E from each discretised element in the domain Ω . Accordingly, the indices i and j refer to global node numbers, where the total number of nodes is denoted by "NbGlob".

It is clear that the global residual inherits the dependence between volumetric enthalpy and temperature. This is shown in [eq. \(1.16\)](#) where the average volume enthalpy is a function of the temperature. It infers that this residual is a non-linear function; therefore minimizing it requires an iterative non-linear algorithm. Our choice settles on the Newton-Raphson method, known for its quadratic convergence speed. A solidification problem can induce severe non-linearities from the release of the latent heat (which itself is temperature and composition dependent) and the variations of the average thermophysical properties of the alloy with respect to temperature, phase fraction and average composition. This algorithm could thus treat such variations. Considering the link between the properties and temperature, [eq. \(1.16\)](#) may be solved either for the average volumetric enthalpy or for the temperature as the nodal unknown, hence both formulations are presented hereafter.

1.3.1 Enthalpy-based approach

The residual is re-written using a Taylor series expansion to the first order for a non-linear iteration (ν) :

$$(R_i)^{(\nu+1)} = (R_i)^{(\nu)} + \left(\frac{dR}{dH} \right)_{ij}^{(\nu)} \Delta H_j^{(\nu)} + \mathcal{O}(H_j^2) \quad (1.17)$$

Neglecting the second order terms, the suggested correction at each iteration in view of cancelling the residual and giving the new value $H_j^{(\nu)}$, is given by the linear system in [eq. \(1.18\)](#) relative to what we call a *Hsolver*:

$$\left(\frac{dR}{dH} \right)_{ij}^{(\nu)} \left(H_j^{(\nu+1)} - H_j^{(\nu)} \right) = -R_i^{(\nu)} \quad (1.18)$$

where $\frac{dR}{dH}$ is a global tangent matrix yielding the variations of the residual with respect to the volumetric enthalpy in the previous iteration, $H_j^{(\nu)}$. The detailed flow chart for the *Hsolver* is given in [section 1.3.3](#). If [eq. \(1.8\)](#) is considered, then the contribution of an element Ω_E writes:

$$\left(\frac{dR^E}{dH} \right)_{ij}^{(\nu)} = \underbrace{\mathcal{M}_{ij}^E + \mathcal{A}_{ij}^E \left(\frac{dT}{dH} \right)_j^{(\nu)}}_{\text{no sum on } j} + \underbrace{(\mathcal{K}1_{ij}^E + \mathcal{K}2_{ij}^E) \left(\frac{dT}{dH} \right)_j^{(\nu)}}_{\text{no sum on } j} \quad (1.19)$$

[Equation \(1.19\)](#) is the core of the enthalpy-based solver. The resolution of [eq. \(1.18\)](#) then yields a new estimate of the vector of nodal volumetric enthalpies $H^{(\nu+1)}$, which are the only unknowns to be solved for. Once determined at iteration (ν) , convergence tests are performed.

1.3.2 Temperature-based approach

Similarly to the *Hsolver*, the local residual is recast for a nonlinear iteration (ν) , leading this time to an iterative temperature correction:

$$\left(\frac{dR}{dT} \right)_{ij}^{(\nu)} \left(T_j^{(\nu+1)} - T_j^{(\nu)} \right) = -R_i^{(\nu)} \quad (1.20)$$

where $\frac{dR}{dT}$ is a global tangent matrix yielding the variations of the residual with respect to temperature $T_j^{(\nu)}$ at the previous iteration. This solver will be referred to as *Tsolver*. The corresponding flow chart is given in [section 1.3.3](#). The contribution of an element

Ω_E to this tangent matrix is evaluated as:

$$\left(\frac{dR^E}{dT}\right)_{ij}^{(\nu)} = \underbrace{\mathcal{M}_{ij}^E \left(\frac{dH}{dT}\right)_j^{(\nu)}}_{\text{no sum on } j} + \mathcal{A}_{ij}^E + (\mathcal{K}1_{ij}^E + \mathcal{K}2_{ij}^E) \quad (1.21)$$

In contrast to the previous solver, [eq. \(1.21\)](#) is the core of the temperature-based solver. The resolution of [eq. \(1.20\)](#) then yields a new estimate of the vector of nodal temperatures $T^{(\nu+1)}$, which are the only unknowns to be solved for. Once updated for iteration (ν) , convergence tests are performed.

1.3.3 Convergence

The previous two sections described the iterative resolution of the same discretised energy conservation by both *Tsolver* and *Hsolver*. However, in [eqs. \(1.19\)](#) and [\(1.21\)](#), an important term emerges from the tangent matrix evaluation describing the variations between enthalpy and temperature: $\frac{dT}{dH}$ and $\frac{dH}{dT}$.

This term invokes the previously mentioned temperature-enthalpy tabulations which depend on the alloy composition. Consequently, $\frac{dT}{dH}$ (respectively $\frac{dH}{dT}$) has a great influence on the convergence of the *Hsolver* (respectively the *Tsolver*). When [eq. \(1.18\)](#) or [eq. \(1.20\)](#) is solved at iteration (ν) , this term is written using a finite difference:

$$\textbf{Hsolver} \quad \left(\frac{dT}{dH}\right)_j^{(\nu+1)} = \frac{T_j^{(\nu+1)} - T_j^{(\nu)}}{\langle \rho h \rangle_j^{(\nu+1)} - \langle \rho h \rangle_j^{(\nu)}} \quad (1.22)$$

$$\textbf{Tsolver} \quad \left(\frac{dH}{dT}\right)_j^{(\nu+1)} = \frac{\langle \rho h \rangle_j^{(\nu+1)} - \langle \rho h \rangle_j^{(\nu)}}{T_j^{(\nu+1)} - T_j^{(\nu)}} \quad (1.23)$$

For the *Tsolver*, the enthalpy $\langle \rho h \rangle_j^{(\nu)}$ is needed to evaluate [eq. \(1.23\)](#). In contrast, the *Hsolver* requires the value of $T_j^{(\nu)}$ to evaluate the corresponding [eq. \(1.22\)](#). In both cases, the unknown is determined by the tabulations. The indices next to the mentioned unknowns indicate that this relation is used for each iteration (ν) at each mesh node j , hence affecting the global resolution time between the two solvers. The *Hsolver* needs a *H2T* to evaluate $\frac{dT}{dH}$, whereas the *Tsolver* needs a *T2H* to evaluate $\frac{dH}{dT}$. It can be seen that *Tsolver* uses solely *T2H* procedure (flowchart in [fig. 1.1](#)) and the thermodynamic tabulations to determine the volumetric enthalpy, hence the term $\frac{dH}{dT}$. On the other hand, *Hsolver* repeats the same procedure a finite number of times in order to determine a temperature output through *H2T* (flowchart in [fig. 1.2](#)) and use it to compute $\frac{dT}{dH}$. This algorithmic difference leverages the *Tsolver* in terms of computa-

tion time providing the same numerical accuracy while conserving the total system energy.

Convergence tests are necessary at the end of each iteration of the energy solver to determine the convergence status of the algorithm. In the context of the *Tsolver* for instance, the residual is re-evaluated with the newly determined temperature $T_j^{(\nu+1)}$ and enthalpy $H_j^{(\nu+1)}$ so [eq. \(1.16\)](#) rewrites:

$$(R_i)^{(\nu+1)} = \mathcal{M}_{ij} \left(H_j^{(\nu+1)} - H_j^{t-\Delta t} \right) + \mathcal{A}_{ij} T_j^{(\nu+1)} + (\mathcal{K}1_{ij} + \mathcal{K}2_{ij}) T_j^{(\nu+1)} - \mathcal{F}_i - \mathcal{Q}_i$$

$$i, j : 1 \rightarrow \text{NbGlob}$$
(1.24)

The norm of the current residual, $\|R^{(\nu+1)}\|$, is compared to a fixed small value $\varepsilon_R \approx [10^{-5}; 10^{-4}]$. The resulting temperature variation, $|T_j^{(\nu)} - T_j^{(\nu-1)}|$, should also respond to similar criterion between two consecutive iterations. For that purpose, we compare it to another fixed value $\varepsilon_T \approx [10^{-3}; 10^{-2}]$. Convergence is ultimately achieved when the following criteria are simultaneously met:

$$\begin{cases} \|R^{(\nu+1)}\| < \varepsilon_R \\ \text{Max}_{j:1 \rightarrow \text{NbGlob}} |T_j^{(\nu+1)} - T_j^{(\nu)}| < \varepsilon_T \end{cases}$$
(1.25)

A comparison of both solver formulations is done in the hereafter test cases section.

1.4 Validation

1.4.1 Pure diffusion

The two solvers are first tested in a purely diffusive case for a one-dimensional solidification configuration. Predictions with a 1D front tracking model [\[Gandin 2000\]](#) is used as a benchmark. It provides solutions for the temperature and solid fraction during directional solidification of a 10 cm long Al-7 wt.% Si ingot. The melt, with initial uniform temperature, is cooled with a heat exchange coefficient (assuming a Fourier boundary condition) from one side, the other side being adiabatic. All values for alloy properties, initial and boundary conditions and numerical parameters are listed in [table 1.2](#). For this simple test case, we use linear temperature dependence of the intrinsic phase enthalpies, that is $\langle \rho h \rangle^s = \rho C_p T$ and $\langle \rho h \rangle^l = \rho (C_p T + L)$, where ρ is the alloy density, C_p is the heat capacity per unit mass and L is the latent heat per unit mass. Values for ρ , C_p and L , as well as for the thermal conductivities, $\kappa = \langle \kappa \rangle^l = \langle \kappa \rangle^s$, are taken constant.

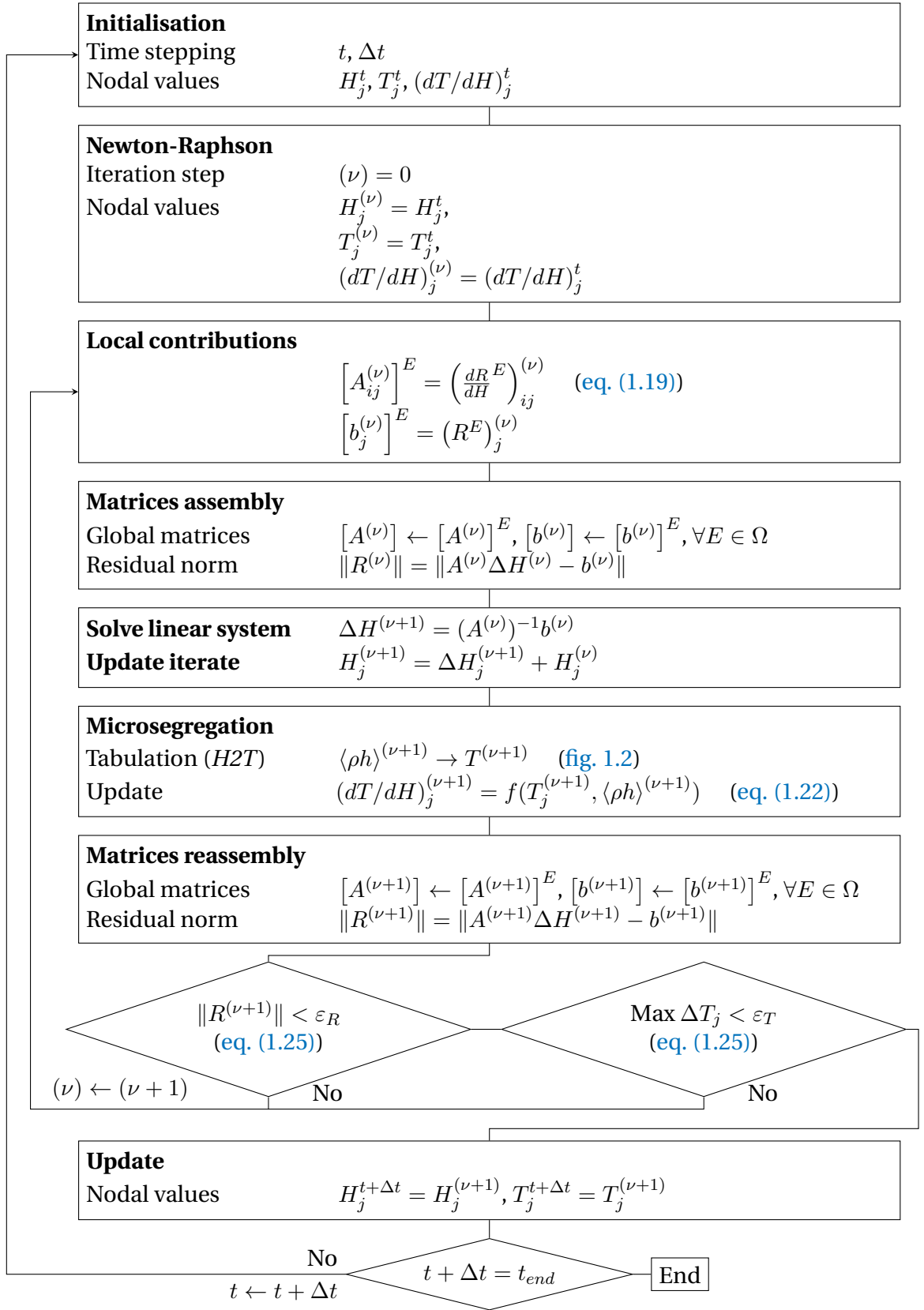


Fig. 1.3 – Resolution algorithm of the enthalpy-based solver.

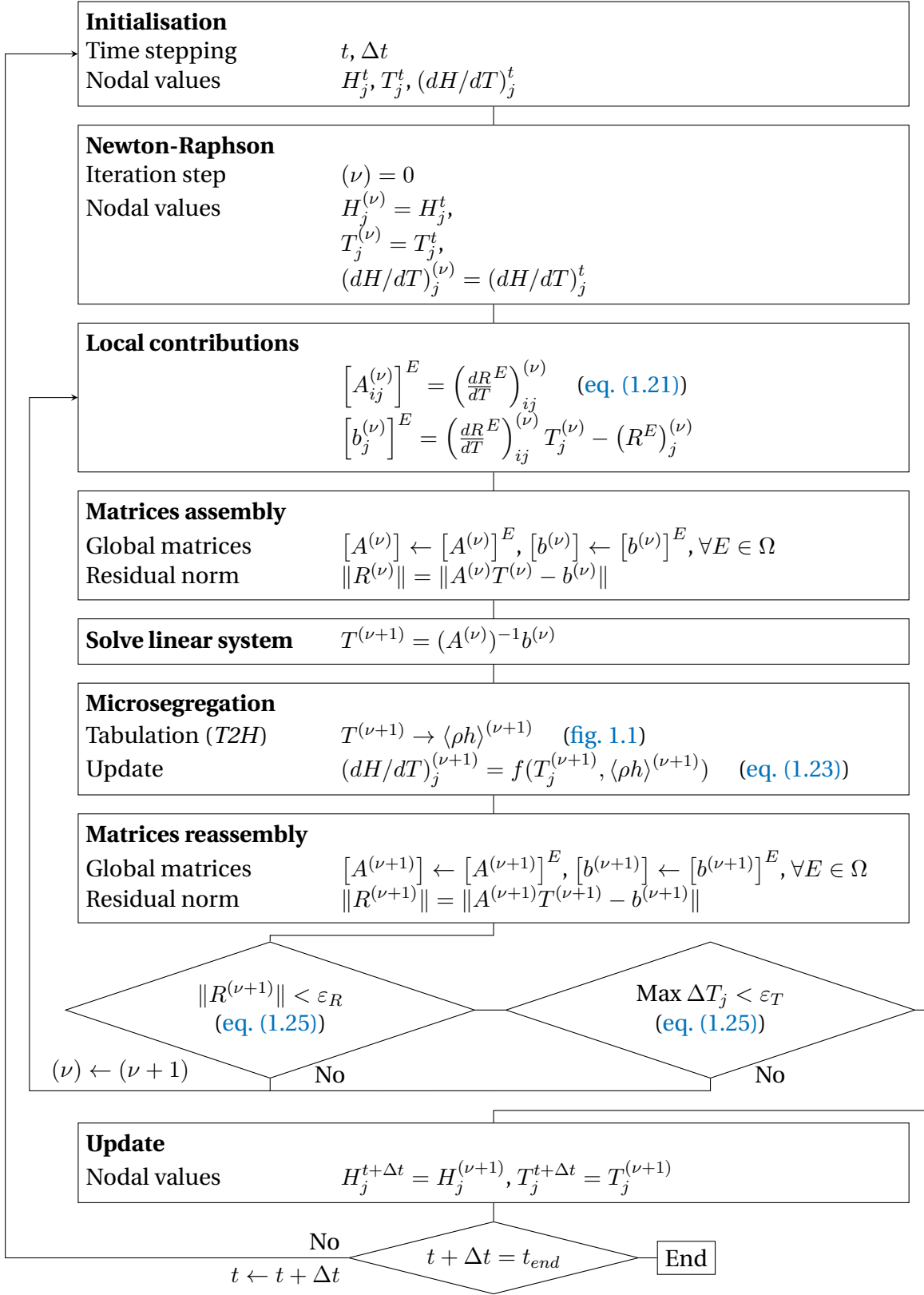


Fig. 1.4 – Resolution algorithm of the temperature-based solver.

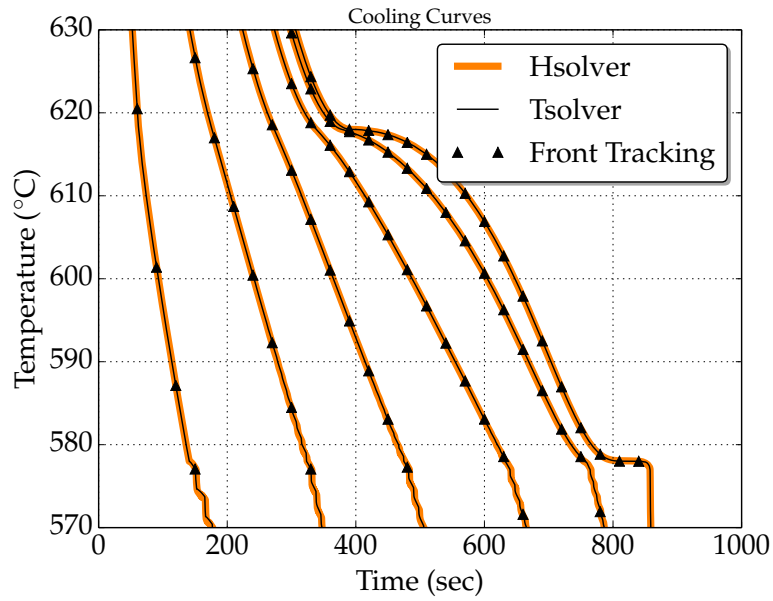
A Gulliver-Scheil approximation is used to compute a single relationship between temperature and volume solid fraction, g^s , in the absence of macrosegregation. This is done assuming a linear binary phase diagram and thus requires using the properties listed in [table 1.2](#), i.e. the segregation coefficient, k , the liquidus slope, m_L , the liquidus temperature, T_L , and the eutectic temperature, T_E . [Figure 1.5](#) show the comparison with the *Hsolver* and *Tsolver*. The cooling curves and liquid fraction results are found superimposed to the front tacking solution, thus giving validation of the implementation as well as the iterative schemes presented above to solve the energy conservation

Table 1.2 – Parameters for the pure diffusion test case with an Al-7 wt.% Si alloy presented in [fig. 1.5](#)

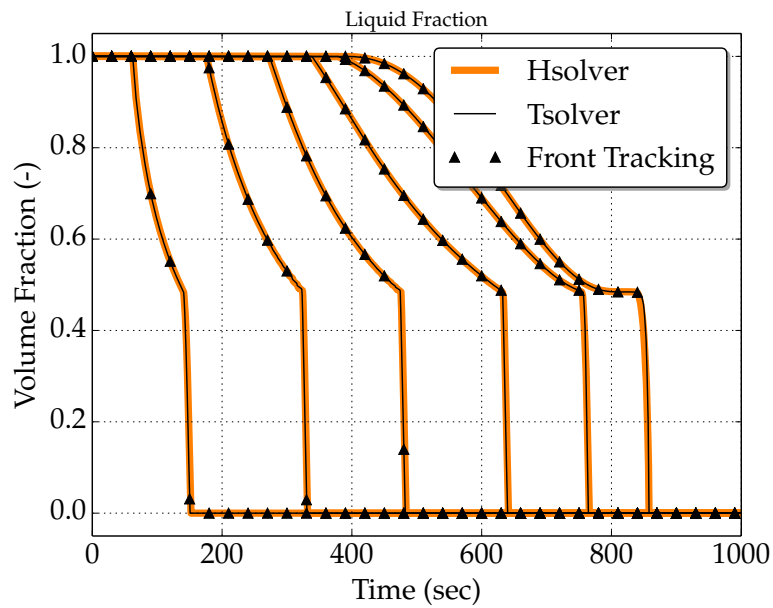
Parameter	Symbol	Value	Unit
Nominal composition	w_0	7	wt. %
Liquidus temperature	T_L	618	°C
Eutectic temperature	T_E	577	°C
Segregation coefficient	k	0.13	—
Liquidus slope	m_L	−6.5	K wt. % ^{−1}
Density	ρ	2600	kg m ^{−3}
Liquid heat capacity	C_p	1000	J kg ^{−1} K ^{−1}
Enthalpy of fusion	L	365 384	J kg ^{−1}
Thermal conductivity	κ	70	W m ^{−1} K ^{−1}
Heat transfer coefficient	h_{ext}	500	W m ^{−2} K ^{−1}
External temperature	T_{ext}	100	°C
Initial temperature	T_0	800	°C
Ingot length		0.1	m
FE mesh size		10 ^{−3}	m
Time step	Δt	0.1	s
Convergence criterion (residual)	ε_R	10 ^{−6}	—
Convergence criterion (temperature)	ε_T	10 ^{−2}	K

1.4.2 Convection and diffusion

To validate the *Tsolver* with fluid flow, we consider the following set of equations already defined in the flowchart of [??](#). Moreover, an assumption of a static and non deformable solid phase is made. Consequently, the mechanical model is reduced to the conservation of momentum in the liquid phase. This assumption also yields some



(a)



(b)

Fig. 1.5 – Computed unidirectional heat diffusion during solidification of an Al-7 wt.% Si alloy using (orange) the enthalpy method and (black) the temperature method, comparison being made for (a) cooling curves and (b) the liquid fraction history. Each curve corresponds to a position along the sample, from 0 cm (cooling side) to 10 cm (insulated side), with 2 cm spacing between the positions.

other consequences on the mass balance and the liquid momentum conservation. In the latter, a Darcy term is added to take into account the dissipative interfacial stress in the porous-like mushy zone. Its main parameter is the permeability of the mushy zone, K . It is considered isotropic, hence reducing to a scalar which is given by the Carman-Kozeny relation, based on the secondary dendrite arm spacing λ_2 : $K = \frac{g^l^3 \lambda_2^2}{180(1-g^l)^2}$. The liquid density being taken constant, its spatial variations as a function of temperature and average composition are still needed to compute thermosolutal convection forces. For that purpose, the Boussinesq approximation (??) is used, considering the thermal β_T and solutal $\beta_{\langle w \rangle^l}$ expansion coefficients and a reference density, ρ_{ref} , defined at a reference temperature T_0 and reference composition w_0^l . Values for the references are taken at the liquidus temperature and the nominal composition of the alloy, $\langle w \rangle_0$ [Carozzani et al. 2013]. More details about the FE formulation can be found in the PhD work of Rivaux [2011] and Carozzani [2012]. The Tsolver's ability to be coupled with

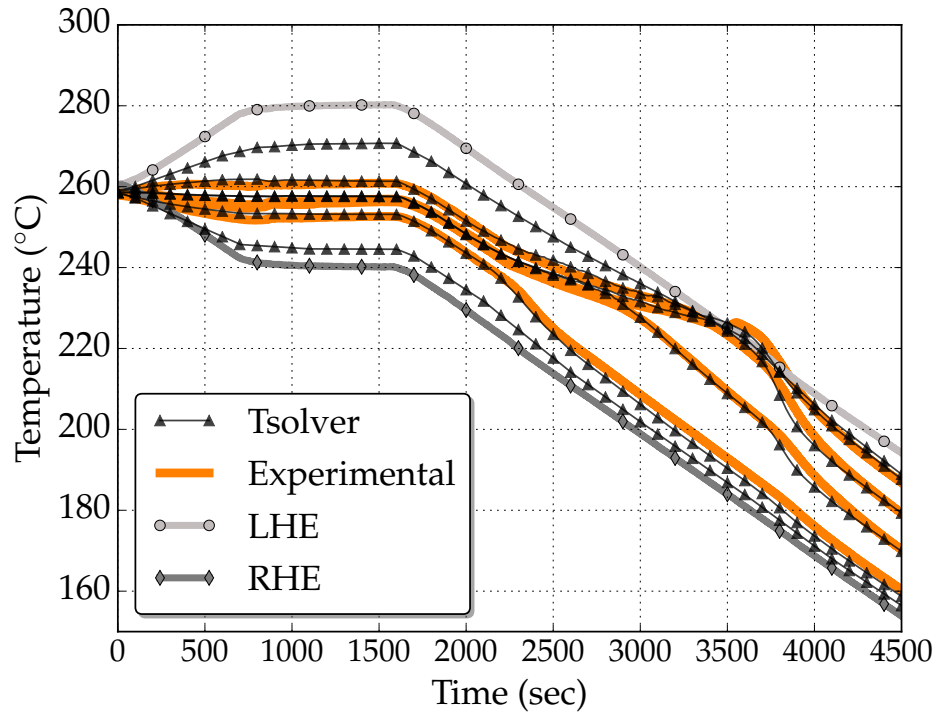


Fig. 1.6 – Experimental cooling curves overlap with the results of the 3D FE convection-diffusion simulation. The left (LHE) and right (RHE) heat exchangers impose the boundary temperature in the experiment.

various physical phenomena like macrosegregation and fluid flow in porous medium is displayed in this test case. Details about fluid flow resolution will not be given in this section, but rather in the next chapter. It consists of a solidification benchmark where a 10 cm width \times 6 cm height \times 1 cm thick cavity containing a Sn-3 wt.% Pb melt

is cooled down from its two narrowest vertical sides using heat exchangers (LHE: left heat exchanger, RHE: right heat exchanger). The experiment, inspired by [Hebditch et al. \[1974\]](#) similar set up, has been revisited by [Hachani et al. \[2012\]](#) who performed the solidification with better controlled conditions and using an increased number of samples for composition analysis. Recently, a successful attempt to simulate the experiment was carried out by [Carozzani et al. \[2013\]](#) relying on an enthalpy resolution. All details regarding geometry, finite element discretization, material properties and boundary conditions can be found in the latter reference. For this computation, solidification paths, phase compositions and phase enthalpies were determined by a thermodynamic module dedicated to equilibrium calculations for binary alloys. The 3D simulation results in [fig. 1.6](#) show a satisfactory agreement with the experimental temperature measurements recorded at mid heights of the cavity and uniformly distributed along its width [[Carozzani et al. 2013](#)]. In fact, simulation results with the *Tsolver* and the *Hsolver* were found to be almost superimposed, as shows [fig. 1.6](#). Further comparison is made between both solvers, as shows [fig. 1.7](#), where the average composition, liquid fraction and temperature fields are extracted from a cut plane halfway through the ingot. On the same figure, if we compare the composition, we notice that the solidified part (right side) has basically the same segregation pattern, while in the convected liquid has a slightly different solute distribution. As for the extent of the mushy zone, we observe that liquid fraction contours are very close, indicating that temperature distributions and interdendritic segregation are also close between both solvers predictions. Regarding the computation, the *Tsolver* resolution proves to be faster than the *Hsolver* used by [Carozzani et al. \[2013\]](#): a process time of 7000s required a computation time of 90 hours 13 minutes compared to 114 hours 21 minutes spent by the enthalpy resolution with 32 cores on the same cluster. The gain factor is about 20%.

1.5 Application: multicomponent alloy solidification

We have shown that the efficiency of the temperature-based resolution resides in its performance when combined with thermodynamic tabulations. A multicomponent alloy consists of at least two solute elements, and therefore the tabulation size increases, hence the number of search operations also increases. To demonstrate the speed-up ability of the temperature-based approach while predicting all phase transformations during macrosegregation caused solely by mass diffusion, we consider the solidification of a ternary alloy, Fe-2 wt.% C-30 wt.% Cr. In order to neglect fluid flow resolution, we assume that solidification in this case is so slow that no forces are gen-

1.5. Application: multicomponent alloy solidification

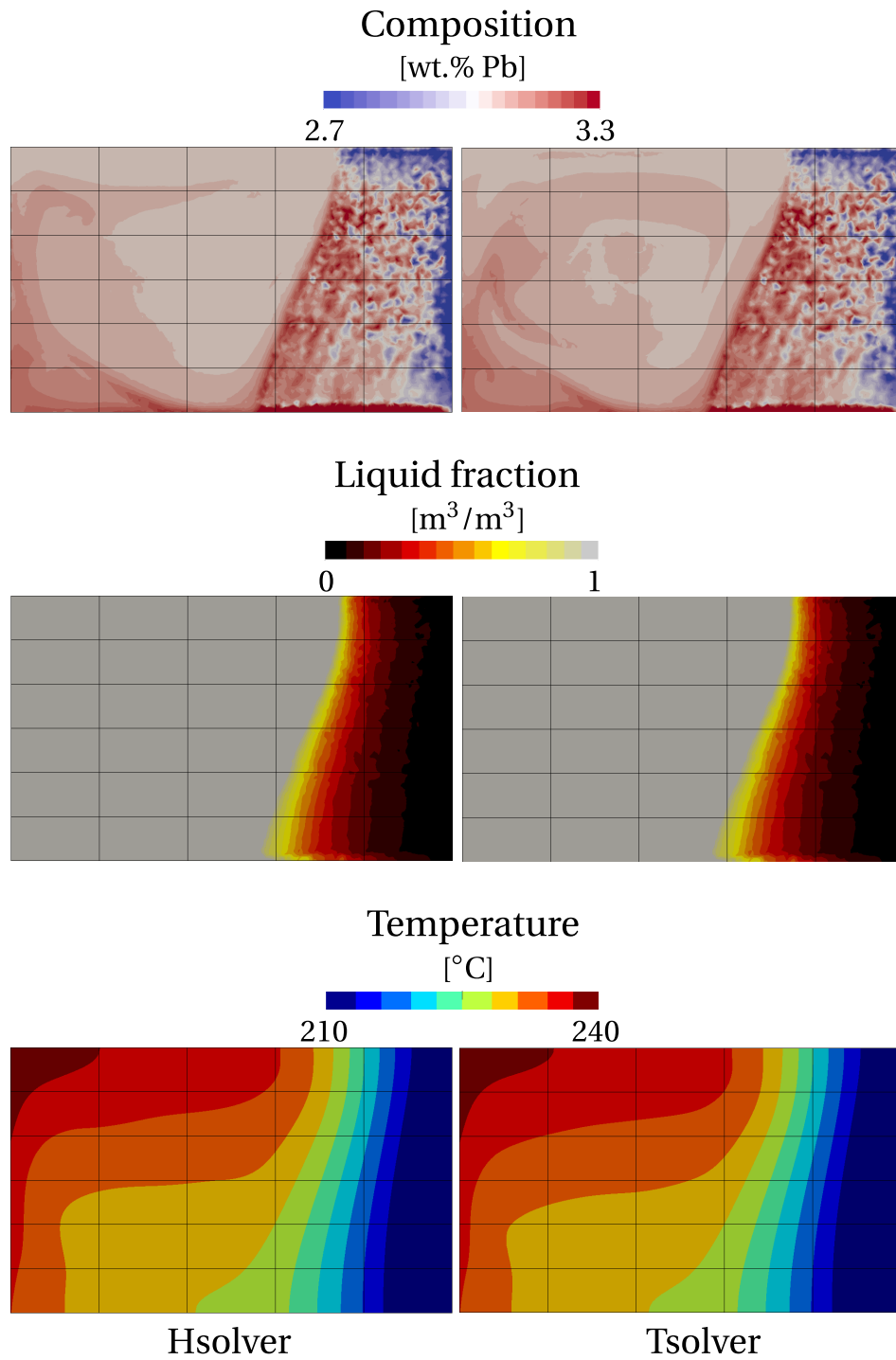


Fig. 1.7 – Comparison of 3D simulation results: average composition, liquid fraction and temperature at $t=3000$ s for *Tsolver* and *Hsolver*.

erated inside the melt, while additionally all buoyancy forces are also neglected, so no momentum conservation is solved in this section. As illustrated in [fig. 1.9a](#), the alloy domain has a cylinder shape close to 3-inch height \times 1-inch diameter. Exact values are reported in [table 1.3](#) with all material properties, initial and boundary conditions, as well as numerical parameters for the simulations. The melt steel is initially at 1395 °C. The temperature of the bottom surface is imposed with a constant decreasing rate of 0.1 K s⁻¹ starting with 1380 °C, i.e. 40 °C higher than the nominal liquidus temperature, as shown in [fig. 1.9b](#). The other surfaces are kept adiabatic. The cylinder is held in a vertical position. [fig. 1.8](#) also provides the transformation path of the alloy at nominal composition, i.e. assuming no macrosegregation and full thermodynamic equilibrium as computed with ThermoCalc and the TCFE6 database [[TCFE6 2010](#); [Andersson et al. 2002](#)]. A total of 5 phases need to be handled, the characteristic temperature for their formation being reported in [fig. 1.9b](#).

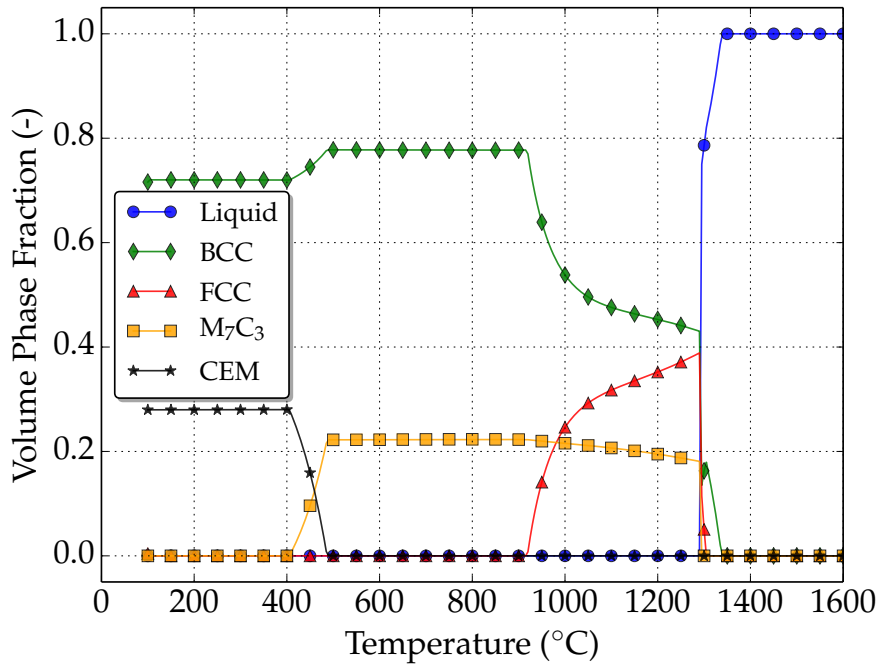


Fig. 1.8 – Thermodynamic mapping [[TCFE6 2010](#); [Andersson et al. 2002](#)] of the transformation path for the Fe-2 wt.% C-30 wt.% Cr at nominal composition.

1.5.1 Tabulations

Full thermodynamic equilibrium is considered in the present case. Due to macrosegregation, the average composition is expected to continuously vary in time and space during casting. Transformation paths are thus determined a priori for a set of average

1.5. Application: multicomponent alloy solidification

compositions around the nominal value. Hence, carbon content varies in the interval [1.8 wt.%, 2.2 wt.%] while chromium content variation is in the interval [27 wt.%, 33 wt.%]. The offset of $\pm 10\%$ with respect to the nominal composition value allows tabulating relatively small composition steps to ensure a fairly accurate mapping when compared to the corresponding ternary phase diagram. The average composition step is 0.04 wt.% for carbon and 0.6 wt.% for chromium, thus representing 2% intervals with respect to the nominal composition. The temperature varies in the interval [100 °C, 1600 °C] by 5 °C steps. For each triplet (carbon content in wt.% C, $\langle w_C \rangle_0$, chromium content in wt.% Cr, $\langle w_{Cr} \rangle_0$, temperature in K) corresponds a phase fraction g^ϕ and a pair of intrinsic phase composition ($\langle w_{Cr} \rangle^\phi, \langle w_C \rangle^\phi$). For the 5 phases listed in [fig. 1.8](#) (LIQ \equiv liquid, BCC \equiv ferrite, FCC \equiv austenite, $M_7C_3 \equiv$ carbide, CEM \equiv cementite), the enthalpy h^ϕ and density ρ^ϕ , are tabulated as functions of temperature and phase intrinsic composition. If this latter input lies between two tabulated values, a linear interpolation is performed to determine the output, i.e. phase enthalpy and density. With the advancement of solidification, the liquid is enriched with solute by macrosegregation, which enables new solidification paths. It means that the primary solidifying phase is not necessarily the same as when considering the nominal composition. For this reason, the tabulation approach is interesting inasmuch as it provides phase transformation paths and values of phase properties that are compatible with the system's actual composition. [Figure 1.10](#) summarizes the tabulated thermodynamic data for two sets of average composition for the considered ternary system. Note that in the present test case, phase densities are taken constant ($\langle \rho \rangle^s = \langle \rho \rangle^l = 6725 \text{ kg m}^{-3}$). Therefore they are not tabulated. With this assumption, no shrinkage occurs upon phase change.

1.5.2 Discussion

A first case is considered without macrosegregation, that is, all mechanical driving forces are bypassed, leading to a static melt. This is achieved by nullifying the thermal and solutal expansion coefficients, which is equivalent to a constant density in space and time, i.e. no Boussinesq force is considered. This way, the average composition may only vary due to diffusion in the liquid phase according to ?? where the convection term is neglected. Diffusion is significantly small in the present case and can be neglected too. In such a case, the composition distribution maintains a homogeneous aspect throughout the sample during the entire cooling sequence. The phase transformations then are necessarily expected to follow the unique path shown in [fig. 1.8](#). After 407 s of cooling, the liquidus isotherm enters the bottom surface of the geometry and starts its upward propagation, marking the solidification onset. [Figure 1.11](#) presents

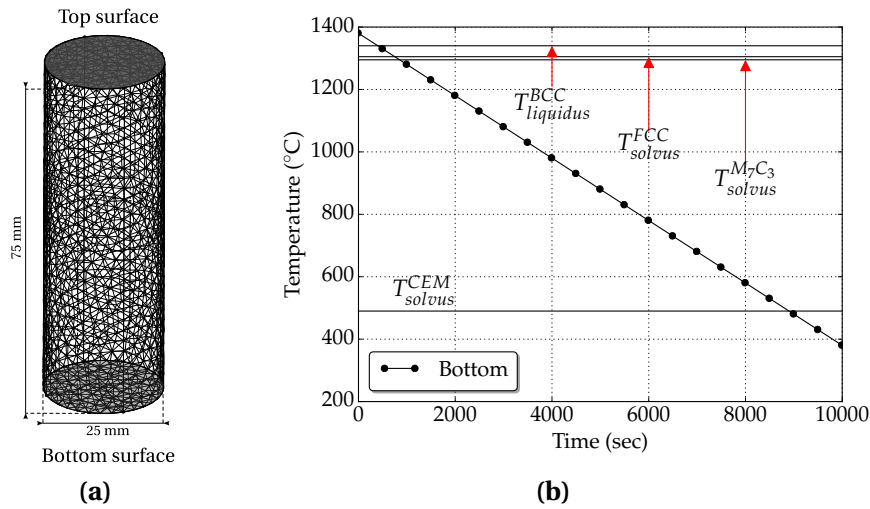


Fig. 1.9 – Configurations for directional casting of (a) a 1 inch diameter \times 3 inches height cylindrical domain for which (b) temperature-time conditions are imposed at its bottom surface.

the simulation results at 3 successive times for the distribution of the solute species and the temperature, as well as for the fraction of phases listed in [fig. 1.8](#). At 600 s, a fully liquid region is still largely present while the mushy zone is made of liquid plus the primary solid phase (ferrite). At 10 560 s, the sample is full solid, with fractions of ferrite and cementite that corresponds to the values read in [fig. 1.8](#) at low temperature. At the selected intermediate time, the presence of 4 phases is found. The solid region at the bottom of the cylinder is made of ferrite, austenite plus carbide, the temperature being still too high to permit the cementite to form. The mushy zone above the solid region is characterized by the presence of 3 phases due to a peritectic reaction taking place that progressively transform ferrite into austenite in the presence of liquid. It can be noticed that the phase fraction isovalues in [fig. 1.11](#) (at 600 s) are horizontal, owing this to two factors: the first is the temperature field, which varies unidirectionally from bottom to top, controlled by thermal diffusion, while the second is the uniform average composition throughout the sample due to the absence of convection. In fact both factors are consequences of the flow absence, which would transport heat and solute by advection, thus inevitably changing the phase distribution. The succeeding phase change is a solid-state transformation where α -ferrite and the carbide M_7C_3 react to form cementite at 490 °C at nominal composition, as shown in [fig. 1.9b](#). The reaction is relatively slow, ending with 28% of cementite and 72% of α -ferrite.

Chapter 1. Energy balance with thermodynamic tabulations

Table 1.3 – Solidification parameters for the Fe-2 wt.% C-30 wt.% Cr alloy.

Parameter	Symbol	Value	Unit
Nominal composition	$\langle w_C \rangle_0$	2	wt. %
	$\langle w_{Cr} \rangle_0$	30	wt. %
Characteristic temperatures	T_{bottom}	fig. 1.9b	°C
Phase fraction	g^ϕ	Tabulations fig. 1.10	—
Phase enthalpy	$\langle h \rangle^\phi$	Tabulations fig. 1.10	—
Phase composition	$\langle w_C \rangle^\phi$	Tabulations fig. 1.10	wt. %
Phase composition	$\langle w_{Cr} \rangle^\phi$	Tabulations fig. 1.10	wt. %
Diffusion coefficients	$\langle D_C \rangle^l$	15×10^{-10}	$\text{m}^2 \text{s}^{-1}$
	$\langle D_{Cr} \rangle^l$	15×10^{-10}	$\text{m}^2 \text{s}^{-1}$
Dynamic viscosity	μ^l	2×10^{-3}	Pa s
Thermal expansion coefficient	β_T	8.96×10^{-5}	K^{-1}
Solutal expansion coefficient	$\beta_{\langle w_C \rangle^l}$	1.54×10^{-3}	wt. \%^{-1}
	$\beta_{\langle w_{Cr} \rangle^l}$	1.72×10^{-2}	wt. \%^{-1}
Thermal conductivity in the solid	$\langle \kappa \rangle^s$	40	$\text{W m}^{-1} \text{K}^{-1}$
Thermal conductivity in the liquid	$\langle \kappa \rangle^l$	28	$\text{W m}^{-1} \text{K}^{-1}$
Dendrite arm spacing	λ	60×10^{-6}	m
Density	ρ_0^l	6725	kg m^{-3}
Reference composition (carbon)	$\langle w_C \rangle_{\text{ref}}^l$	2	wt. %
Reference composition (chromium)	$\langle w_{Cr} \rangle_{\text{ref}}^l$	30	wt. %
Reference temperature	$\langle w_C \rangle_{\text{ref}}^l$	1377	°C
Initial temperature	T_0	1395	°C
Ingots diameter		25×10^{-3}	m
Ingots length		75×10^{-3}	m
FE mesh size		10^{-3}	m
Time step	Δt	0.1	s
Convergence criterion (residual)	ε_R	10^{-6}	—
Convergence criterion (temperature)	ε_T	10^{-2}	K

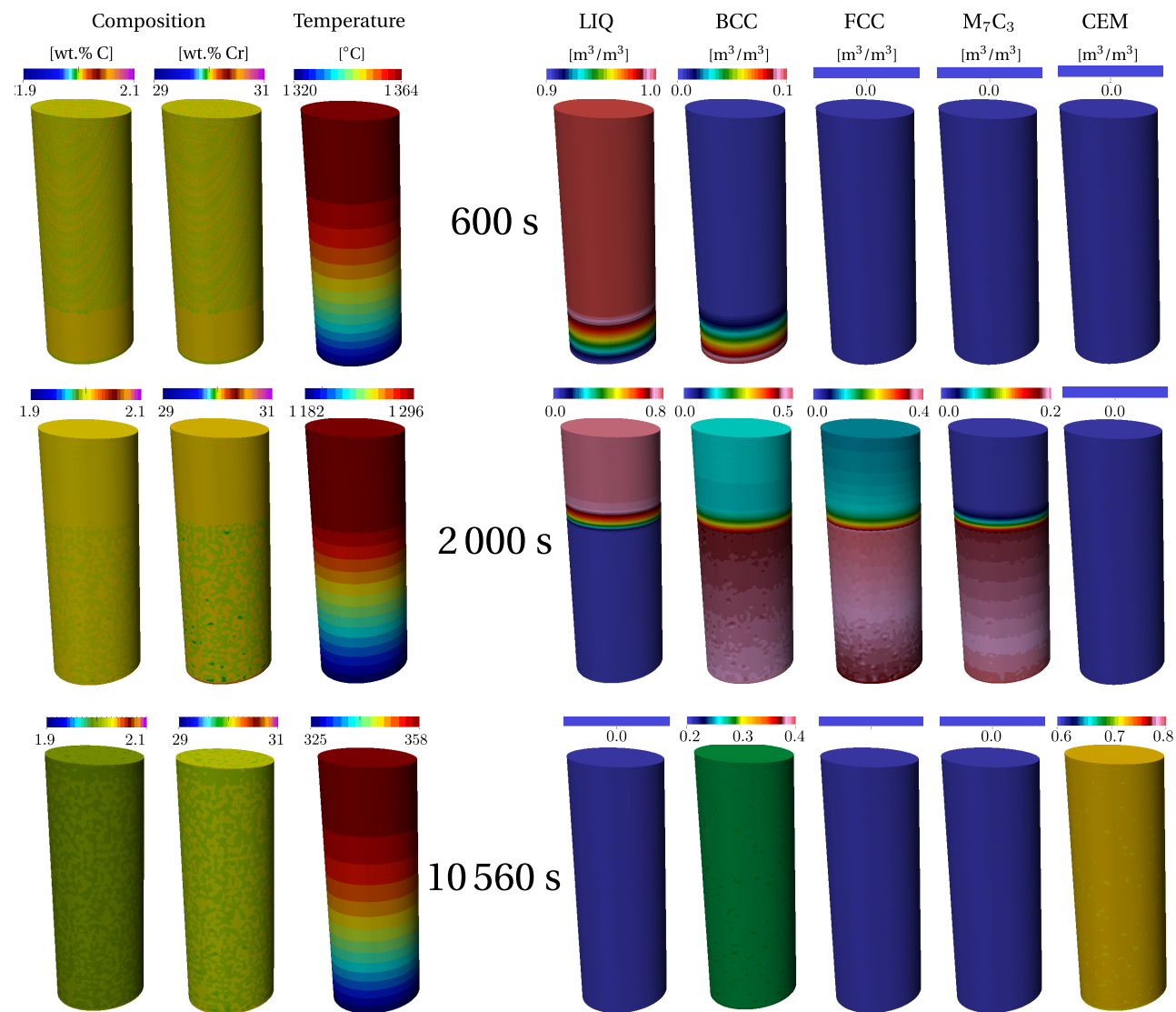


Fig. 1.11 – : Upward solidification of a cylinder rod with a static liquid at 3 stages in a Fe-2 wt.% C-30 wt.% Cr. The left columns show the average composition and temperature distribution, while the right columns show the phase fractions.

Bibliography

[Andersson et al. 2002]

Andersson, J.-O., Helander, T., Höglund, L., Shi, P., and Sundman, B. (2002). “Thermo-Calc & DICTRA, computational tools for materials science”. *Calphad*, 26 (2), pp. 273–312. URL: <http://www.sciencedirect.com/science/article/pii/S0364591602000378> (cited on pages 20, 23).

[Bellet et al. 2009]

Bellet, M. et al. (2009). “Call for contributions to a numerical benchmark problem for 2D columnar solidification of binary alloys”. *International Journal of Thermal Sciences*, 48 (11), pp. 2013–2016. URL: <http://www.sciencedirect.com/science/article/pii/S129007290900177X> (cited on page 2).

[Carozzani et al. 2013]

Carozzani, T. et al. (2013). “Direct Simulation of a Solidification Benchmark Experiment”. *Metallurgical and Materials Transactions A*, 44 (2), pp. 873–887. URL: <http://link.springer.com/article/10.1007/s11661-012-1465-1> (cited on pages 2, 17, 18).

[Carozzani 2012]

Carozzani, T. (2012). “Développement d’un modèle 3D Automate Cellulaire-Éléments Finis (CAFE) parallèle pour la prédiction de structures de grains lors de la solidification d’alliages métalliques”. PhD Thesis. Ecole Nationale Supérieure des Mines de Paris. URL: <http://pastel.archives-ouvertes.fr/pastel-00803282> (cited on page 17).

[Doré et al. 2000]

Doré, X., Combeau, H., and Rappaz, M. (2000). “Modelling of microsegregation in ternary alloys: Application to the solidification of Al–Mg–Si”. *Acta Materialia*, 48 (15), pp. 3951–3962. URL: <http://www.sciencedirect.com/science/article/pii/S1359645400001774> (cited on page 2).

[Du et al. 2007]

Du, Q., Eskin, D. G., and Katgerman, L. (2007). “Modeling Macrosegregation during Direct-Chill Casting of Multicomponent Aluminum Alloys”. *Metallurgical and Materials Transactions A*, 38 (1), pp. 180–189. URL: <http://link.springer.com/article/10.1007/s11661-006-9042-0> (cited on page 2).

[Gandin 2000]

Gandin, C. A. (2000). “From constrained to unconstrained growth during directional solidification”. *Acta Materialia*, 48 (10), pp. 2483–2501. URL: <http://www.sciencedirect.com/science/article/pii/S1359645400000707> (cited on page 12).

Bibliography

[Hachani et al. 2012]

Hachani, L. et al. (2012). "Experimental analysis of the solidification of Sn-3 wt.%Pb alloy under natural convection". *International Journal of Heat and Mass Transfer*, 55 (7–8), pp. 1986–1996. URL: <http://www.sciencedirect.com/science/article/pii/S0017931011007009> (cited on page 18).

[Hebditch et al. 1974]

Hebditch, D. J. and Hunt, J. D. (1974). "Observations of ingot macrosegregation on model systems". *Metallurgical Transactions*, 5 (7), pp. 1557–1564. URL: <http://link.springer.com/article/10.1007/BF02646326> (cited on page 18).

[Rappaz et al. 2003]

Rappaz, M., Bellet, M., and Deville, M. (2003). *Numerical Modeling in Materials Science and Engineering*. Springer Series in Computational Mathematics. Springer Berlin Heidelberg (cited on pages 3, 8).

[Rivaux 2011]

Rivaux, B. (2011). "Simulation 3D éléments finis des macroségrégations en peau induites par déformations thermomécaniques lors de la solidification d'alliages métalliques". PhD Thesis. École Nationale Supérieure des Mines de Paris. URL: <http://pastel.archives-ouvertes.fr/pastel-00637168> (cited on page 17).

[Swaminathan et al. 1993]

Swaminathan, C. R. and Voller, V. R. (1993). "On The Enthalpy Method". *International Journal of Numerical Methods for Heat & Fluid Flow*, 3 (3), pp. 233–244. URL: <http://www.emeraldinsight.com/journals.htm?articleid=1665561&show=abstract> (cited on page 2).

[Süli 2000]

Süli, E. (2000). *Lecture Notes on Finite Element Methods for Partial Differential Equations* (cited on page 6).

[TCFE6 2010]

TCFE6 (2010). *TCFE6: a thermodynamic database for different kinds of steels and Fe-based alloys*. Stockholm, SE. URL: <http://goo.gl/qiD3kE> (cited on pages 20, 23).

[Thuinet et al. 2004]

Thuinet, L. and Combeau, H. (2004). "Prediction of macrosegregation during the solidification involving a peritectic transformation for multicomponent steels". *Journal of Materials Science*, 39 (24), pp. 7213–7219. URL: <http://link.springer.com/article/10.1023/B%3AJMSC.0000048734.34597.1e> (cited on page 2).